

Magnon-assisted tunnelling in van der Waals heterostructures based on CrBr₃

D. Ghazaryan¹, M.T. Greenaway², Z. Wang¹, V.H. Guarochico-Moreira^{1,3}, I.J. Vera-Marun¹, J. Yin¹, Y. Liao¹, S. V. Morozov^{4,5}, O. Kristanovski⁶, A. I. Lichtenstein⁶, M. I. Katsnelson⁷, F. Withers⁸, A. Mishchenko^{1,9}, L. Eaves^{1,10}, A. K. Geim^{1,9}, K. S. Novoselov^{1,9,}, A. Misra¹*

¹*School of Physics and Astronomy, University of Manchester, Oxford Road, Manchester, M13 9PL, UK*

²*Department of Physics, Loughborough University, Loughborough, LE11 3TU, UK*

³*Escuela Superior Politécnica del Litoral, ESPOL, Facultad de CNM, Campus Gustavo Galindo Km 30.5 Vía Perimetral, P.O. Box 09-01-5863, Guayaquil, Ecuador*

⁴*Institute of Microelectronics Technology and High Purity Materials, RAS, Chernogolovka, 142432, Russia*

⁵*National University of Science and Technology "MISiS", 119049, Leninsky pr. 4, Moscow, Russia*

⁶*Institute of Theoretical Physics, University Hamburg, D-20355, Hamburg, Germany*

⁷*Institute for Molecules and Materials, Radboud University, 6525AJ, Nijmegen, Netherlands*

⁸*University of Exeter, College of Engineering, Mathematics and Physical Sciences, Exeter EX4 4SB, Devon, England*

⁹*National Graphene Institute, University of Manchester, Oxford Road, Manchester, M13 9PL, UK*

¹⁰*School of Physics and Astronomy, University of Nottingham, Nottingham, NG7 2RD, UK*

The growing family of two-dimensional (2D) materials that are now available¹⁻³ can be used to assemble van der Waals heterostructures with a wide range of properties⁴⁻⁶. Of particular interest are tunnelling heterostructures⁷⁻⁹, which have been used to study the electronic states both in the tunnelling barrier and in the emitter and collector contacts^{10,11}. Recently, 2D ferromagnets have been studied theoretically¹²⁻¹⁵ and experimentally^{16,17}. Here we investigate electron tunnelling through a thin (2-6 layers) ferromagnetic CrBr₃ barrier. For devices with non-magnetic barriers, conservation of momentum can be relaxed by phonon-assisted tunnelling^{8,18-20} or by tunnelling through localised states^{8,20,21}. In the case of our ferromagnetic barrier the dominant tunnelling mechanisms are the emission of magnons at low temperatures or scattering of electrons on localised magnetic excitations above the Curie temperature. Tunnelling with magnon emission offers the possibility of injecting spin into the collector electrode.

Our devices were assembled on an oxidised silicon wafer by the dry transfer method in an inert atmosphere. The layer structure of our devices is Si/SiO₂/hBN/Gr/CrBr₃/Gr/hBN; here Gr stands for graphene, see Fig. 1a. The typical area of the devices is a few tens of square microns. We prepared a number of devices with different numbers $N=2, 4$ and 6 of CrBr₃ monolayers. A tunnel current, I , flows when a bias voltage, V_b , is applied across the two graphene layers. A typical plot of differential conductance $G=dI/dV_b$ is presented in Fig. 1b. The zero-bias conductance depends exponentially on the barrier thickness, see Fig. 1c.

The dependence of G on the applied gate (V_g) and bias voltages for a sample with 6 CrBr₃ monolayers is presented as a colour map in Fig. 1b. In previously studied devices with hBN barriers, the passage of the Fermi level through the zero in the density of states at the Dirac points of the top and bottom graphene electrodes is observed as an X-shaped feature in the colour map^{10,11,18,22}, where $G=0$. This feature is not observed in the devices with a CrBr₃ barrier. We attribute this to a high level of doping of the graphene electrodes by the CrBr₃.

A magnetic field, B_{\perp} applied perpendicular to the layers (i.e. parallel to the tunnel current) causes the electron spectrum to quantise into a series of Landau levels (LL). In Fig. 1d the Landau quantisation is revealed in $G(V_b, V_g)$ as a series of parallel stripes, with positive slope, due to the passage of the chemical potential through the gaps between LLs. Only this series of peaks with a positive slope is observed, corresponding to Landau quantization in the lower graphene electrode. The absence of stripes with a negative slope that would arise from LLs in the top electrode indicates that the CrBr₃ layer screens the gate voltage-induced electric field so that the chemical potential in the top graphene layer is unchanged by V_g .

Figures 1b,e reveal a series of step-like increases of the tunnel conductance, with values of V_b that are independent of the gate voltage. This type of behaviour is characteristic of inelastic tunnelling with phonon emission and has been observed previously for Gr/hBN/Gr tunnel junctions^{8,18-20}. When the two graphene electrodes of the device are crystallographically misaligned, in-plane momentum conservation requires that the tunnelling electrons are scattered by impurities or by the emission of a phonon¹⁰.

In order to identify the quasiparticles responsible for inelastic tunnelling events in the CrBr₃ devices, we measure G as a function of magnetic field parallel to the layers, B_{\parallel} , (perpendicular to the tunnelling current), see Fig. 1e. In this geometry LL quantisation of the electrons in graphene is absent. The measured resistance of the device contacts is almost completely independent of applied magnetic field; therefore, any change in position of a particular feature in conductance must be due to a change in the tunnel mechanism. In Fig. 1e and f some of the peak positions are clearly dispersed in V_b by the applied magnetic field, whereas others are not. We attribute the non-dispersed peaks to phonon-assisted tunnelling^{8,18-20} and the dispersed peaks to magnon-assisted tunnelling²³. The dispersing peaks are shifted linearly with B_{\parallel} , with a slope of between $(5.1 \pm 0.25) \cdot \mu_B$ eV/T and $(5.7 \pm 0.2) \cdot \mu_B$ eV/T, depending on the particular peak, here $\mu_B = 5.79 \times 10^{-5}$ eV/T is the electron Bohr magneton.

The calculated density of magnon states in CrBr₃, based on experimentally measured exchange parameters^{24,25}, is shown in Fig 1g. The two van Hove singularities in the spectrum at 8.5 meV and 17 meV arise from the hexagonal symmetry of the CrBr₃ lattice. We relate these peaks to the two step-

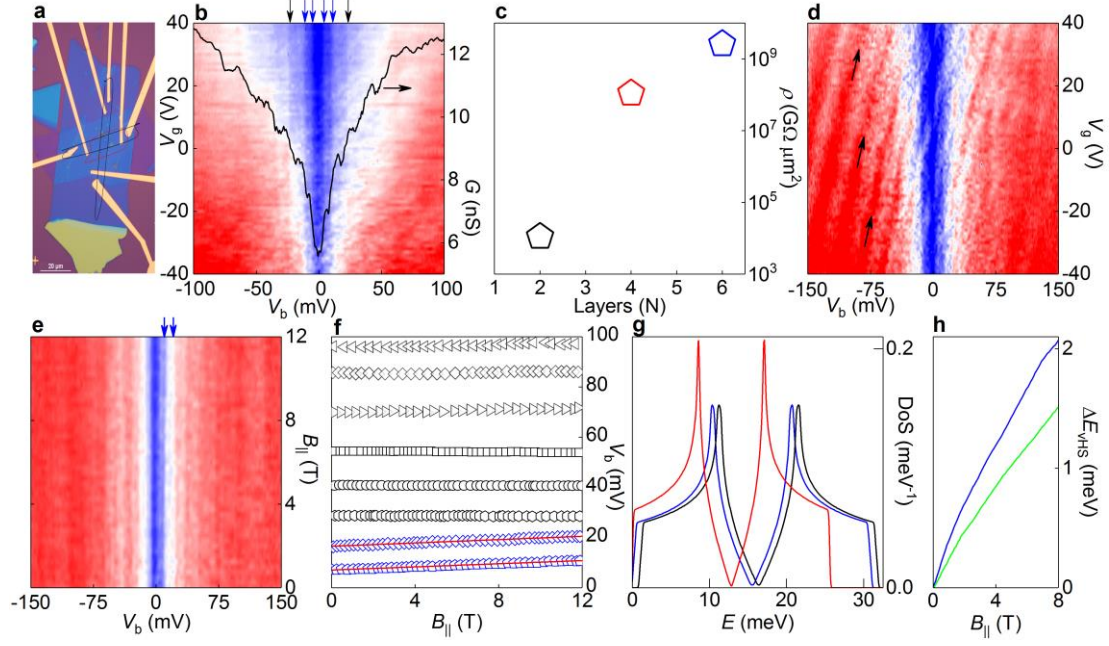


Figure 1| Inelastic magnon assisted tunneling. **a**, Optical micrograph of the investigated device. Black and red contours outline the graphene and CrBr₃ flakes, respectively. Scale bar - 20μm. **b**, Zero-field differential tunneling conductance G dependence on the gate and bias voltages (colour scale is blue to white to red, 6nS to 11.5nS to 17nS) for a 6 layer CrBr₃ tunnel barrier device. Black curve is the tunneling conductance when $V_g=0V$. The arrows indicate some of the step-like increase in G which corresponds to inelastic tunneling with the emission of a magnon (blue) phonon (black). **c**, Zero bias resistivity of junctions with different barrier thicknesses. **d**, as **b**, in perpendicular field of $B_{\perp}=12.5T$. Black arrows correspond to peaks in conductance due to LL spectrum. Colour scale is blue to white to red, 6nS to 12nS to 19nS. **e**, Differential tunneling conductance G as a function of $B_{||}$ and V_b ($V_g=0V$). Colour scale is blue to white to red, 6nS to 12nS to 19nS. **f**, Bias position of the step-like features in G as a function of $B_{||}$. Red lines are the linear fitting with the slopes (from bottom to top) $(5.7\pm0.25)\cdot\mu_B$ eV/T, $(5.1\pm0.2)\cdot\mu_B$ eV/T. **g**, Calculated magnon density of states for $T=10K$, $B=0T$ (blue line), $T=10K$, $B=6.25T$ (black line), $T=T_C$, $B=0T$ (red line). Same calculations provide $T_C=88K$. **h**, Calculated changes of the position of the van Hove singularities in magnon density of states (**g**) as a function of magnetic field for temperatures close to T_C . Green curve – for the peak at 8.5meV at $B=0T$, blue – 17meV at $B=0T$.

like increases in G observed in the experiment at low bias when $V_b \approx 7.5$ mV and 17mV (see Fig. 1b). Previously reported inelastic neutron scattering studies of magnons in CrBr₃ are in a good agreement with our calculations and indicate that the magnon energy is limited to about 30meV^{24,25}. This supports our assumption that non-dispersing steps in G at energies above 30meV should be attributed to phonon-assisted tunnelling.

In a magnetic field, the Zeeman effect would shift the whole magnon spectrum by an energy $2\mu_B B$, along with the two van Hove singularities (Fig. 1g). In the regime of low temperature and high magnetic field, self-consistent spin-wave calculations²⁶ predict a larger shift of the van Hove singularities of $\sim 2.4\mu_B$ eV/T. This enhanced shift of the magnon spectrum is due to magnon-magnon interactions, as explained in detail in the supplementary information. However, the observed magnetic field-induced shift of the position of the steps in conductance of $\sim 5\mu_B$ eV/T, is approximately twice larger than that expected by our theory. Currently, we have no explanation for this discrepancy; understanding it will be the subject of future work. However, we note that at low B and temperatures close to T_C , our self-consistent spin-wave calculations, predict a magnetic field-induced shift in the two Van Hove singularities of $4.5\mu_B$ eV/T and $7.1\mu_B$ eV/T respectively (Fig. 1h and Supplementary Information) which is comparable to the shift measured in our experiments. Such

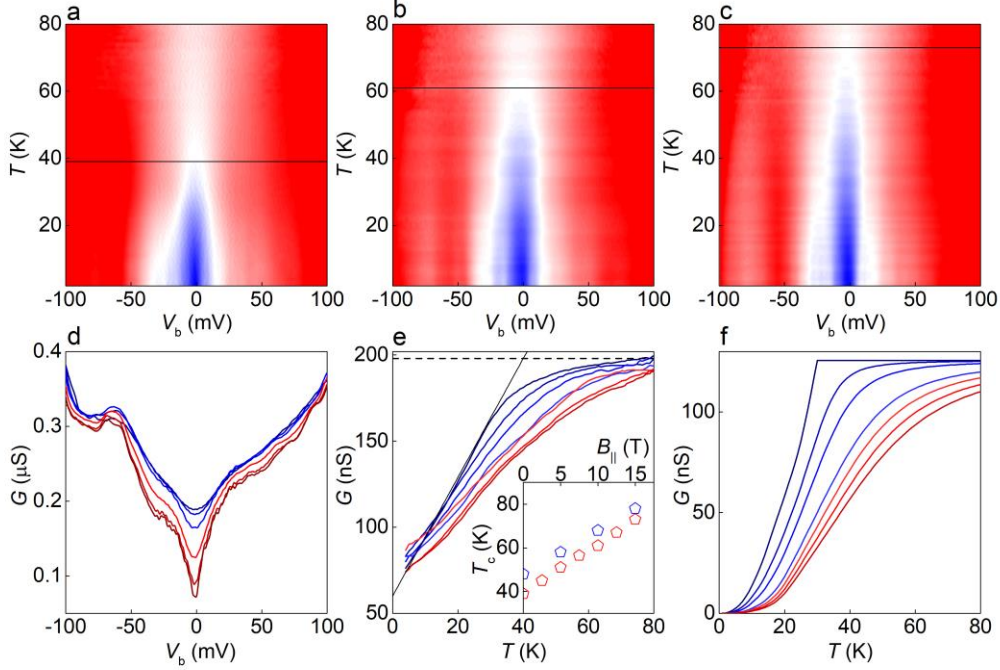


Figure 2] Effect of conductance on in-plane magnetic field. a-c, $G(V_b, T)$ when $V_g=0V$ and $B_{||}=0T$ (a), $B_{||}=10T$ (b), and $B_{||}=15T$ (c) for a device with 4 layer thick CrBr_3 tunnel barrier (colour scale blue to white to red, $0.06\mu S$ to $0.17\mu S$ to $0.3\mu S$ for all contour plots in the figure). Black horizontal lines in a,b,c mark the extracted value of T_c . d, Zero-field tunneling conductance plots for various temperatures at a fixed gate voltage of $V_g=0V$ (blue to purple curves range from $T=2K$ to $T=50K$ with the step $10K$). e, Dependence of the zero bias tunneling conductance G on T for different $B_{||}$ (purple to blue curves ranges between $B_{||}=0T$ and $B_{||}=15T$ with a $2.5T$ increment). Straight lines are guide for an eye and illustrate the method for extraction of the Curie temperature (plotted for $B_{||}=0T$). The dashed black horizontal line illustrates the saturating conductance at the high temperatures, and the straight line indicates the tangent to the particular curve. Inset: The extracted dependence of the T_c on $B_{||}$. Red and blue symbols are for devices with the thickness of the CrBr_3 barrier 4 and 6 layers respectively. f, Theoretical modelling of the zero bias tunneling conductance G dependence on T for different $B_{||}$ (purple to blue curves ranges between $B_{||}=0T$ and $B_{||}=15T$ with a $2.5T$ increment).

strong dependence of magnon spectra on magnetic field close to T_c can be understood as following. The reason of strong dependence of the magnon frequencies on temperature is that both long- and short-range magnetic order being suppressed by spin fluctuations. Both interlayer exchange interactions and Zeeman gap in magnon spectrum suppress the fluctuations, making magnons harder. The change of the regime corresponds to the condition $2\mu_B B \approx J_L$ (J_L is the exchange integral between the layers) which is indeed seen as the change of the slope on the calculated dependence of the energy position of the van Hove singularities on the magnetic field at low B , Fig. 1h.

We now consider the dependence of the differential conductance on temperature, T . Figs. 2a,d plot G as a function of V_b and T . We observe that the zero-bias differential conductance, $G_0=G(V_b=0)$, increases with increasing temperature. Its rate of change, dG_0/dT , is largest for temperatures between 15-30K and saturates above 40K, close to the Curie temperature, $T_c \approx 35K^{24,27}$, for CrBr_3 , Fig. 2e. This behaviour is similar for devices with different CrBr_3 barrier thicknesses (see Supplementary Information) and we attribute it to an increase of elastic scattering of tunnelling electrons with

temperature. We also measure the dependence of G on bias voltage and temperature for different $B_{||}$, Fig. 2a-c. In all cases dG_0/dT decreases with increasing $B_{||}$, Fig. 2e.

At temperatures close to T_c the short-range magnetic ordering *between* the layers and the long-range magnetic ordering *within* the CrBr_3 layer are destroyed as described by the self-consistent spin wave theory of quasi-two-dimensional magnets^{26,28}. The correlation length $\xi(T)$ within the layers is estimated to be

$$\frac{a}{\xi(T)} = \sqrt{\frac{2|\mu|}{3J\gamma}},$$

where a is the nearest-neighbour distance between magnetic atoms, $J\gamma$ is the renormalized in-plane exchange interaction, and μ is the chemical potential of the self-consistent spin waves (see Supplementary Information). Furthermore, at these temperatures the magnon population is very high, so absorption of a magnon by a tunnelling electron is likely.

These observations suggest two possible mechanisms for elastic tunnelling with momentum conservation at zero bias. First, consider a two-magnon process. In the case of a ferromagnetic barrier, emission of two magnons by a tunnelling electron is forbidden by spin conservation. However, a three-particle process is possible in which an electron emits one magnon and absorbs another. This type of process does not change the energy of the electron, changing only its momentum, thus ensuring momentum conservation for electrons tunnelling between the Dirac cones of the two misoriented graphene layers. The ratio between the intensities of the magnon emission (Stokes) and absorption (anti-Stokes) processes is given by $\exp(E_m/k_B T)$, where E_m is the magnon energy and k_B is the Boltzmann constant. At low temperatures, absorption processes are suppressed. However, close to T_c and for our range of parameters, the typical magnon energies is of $\sim k_B T_c$. In 3D magnets with $S \approx 1$, typical magnon energy are of the order of $k_B T_c$ since they are both proportional to zJ , where $z=3$ is the nearest-neighbor number. For 2D magnets, T_c is suppressed by a factor $\sim 1/\ln(J/J_L)$ (see²⁶ for explicit relations) but in our case $J/J_L \approx 10$ and the suppression factor is of the order of unity. This makes the three particle Stokes-anti-Stokes processes significant.

A second potential elastic scattering mechanism, which becomes dominant for $T \sim T_c$, is electron scattering on the imperfections in the spin texture within a CrBr_3 layer^{29,30}. These imperfections break translational symmetry and are capable of scattering the momentum of electron by $1/\xi(T)$. According to our calculations, for temperatures close to T_c , the correlation length falls to values $\sim 10a$, and to $\sim 2a$ at $T \sim 1.5T_c$ (see the Supplemental information). This length scale is much smaller than the de Broglie wavelength of the tunnelling electrons, which is of the order of tens or even hundreds interatomic distances for the case of graphene under the measurement conditions reported here. Hence close to and above T_c tunnelling electrons encounter a highly disordered spin configuration; short range order is lost entirely for $T > T_c$ ²⁸. Scattering of electrons on the short-range spin disorder is therefore analogous to the electron scattering on charged impurities, thereby ensuring momentum conservation for electrons tunnelling between misaligned graphene layers.

We model the elastic tunnelling rate at zero bias by calculating the scattering rate due to two magnon processes at low temperatures ($T \lesssim T_c$) and scattering arising from spin imperfections in the ferromagnet at high temperatures ($T \gtrsim T_c$). For $T \lesssim T_c$, elastic scattering is dominated by two-magnon processes with a rate, W_{2mag} , proportional to the contribution of the longitudinal spectral density^{31,32}

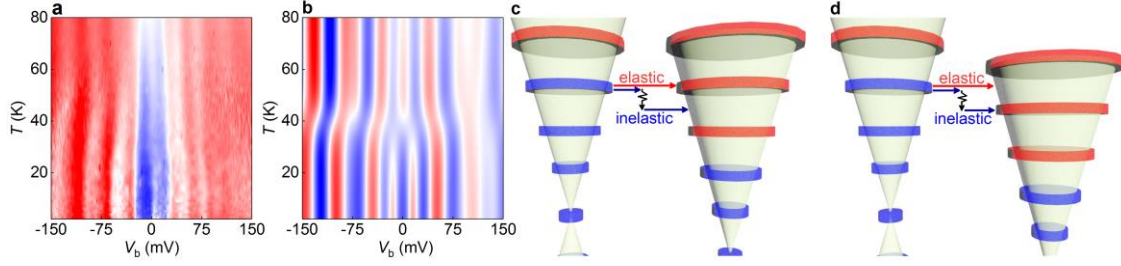


Figure 3 | Inter-LL tunnelling. **a**, measured and **b**, calculated $G(V_b, T)$ when $V_g=0V$ and $B_{\perp}=17.5T$ for a device with 6 layer $CrBr_3$ barrier (colour scale blue to white to red, 4nS to 13nS to 22nS). **c,d**, Schematic diagrams of inelastic and elastic tunnelling events between the LL spectrum of the two graphene layers. Blue states are occupied, red – empty. At low temperatures the tunnelling is inelastic (blue arrows) with magnon emission (black arrow). Increasing temperature increases the contribution to the current of elastic two magnon and spin disorder scattering (red arrows). Application of a bias voltage differentiates between these two processes, in **c** the bias is such that elastic processes allows resonant tunnelling between the 3rd and 4th LLs. In **d** the bias is higher, which brings the same 3rd and 4th LLs into resonance, but is now mediated by inelastic tunnelling.

(also see Supplementary Information). For $T \gtrsim T_c$, the elastic tunnelling rate, W_{spin} , is dominated by scattering on the disordered spin texture^{29,30}, and is therefore dependent on the magnetisation of the ferromagnet³³. We combine the two scattering rates by smoothly varying the amplitudes of the two scattering rates to reflect the increase in the thermal spin disorder of the lattice, so that $W_{tot} = (1 - f(T)) W_{2mag} + f(T) W_{spin}$ where $f(T) = 0.5[1 + \tanh(\alpha(T/T_c - 1))]$. We obtain a good fit to the data when $\alpha=4$, see Fig 2f.

The measured magnetic field-dependence of the conductance also fits well to our model: as the external magnetic field increases, the magnon energy increases due to the Zeeman effect (Fig. 1g), thus reducing the magnon population and the rate W_{2mag} at a given T . At high temperatures, the external magnetic field contributes to spin alignment, thus reducing scattering by imperfections of the spin texture.

Finally, we consider the effect of B_{\perp} on G as a function of bias and temperature. Tunnelling between the LLs of the two graphene layers give rise to peaks in G , see Fig. 3a. As T approaches T_c we observe a clear shift in the position of the peaks in V_b . We interpret this behaviour as a transition from inter-LL tunnelling dominated by inelastic transitions to tunnelling dominated by elastic transitions, as illustrated in the band diagrams, Fig. 3c and d, where inelastic and elastic tunnelling processes are depicted by blue and red arrows respectively.

For inelastic tunnelling, an electron in the 3rd LL of the bottom electrode cannot tunnel with the emission of a magnon since its reduced energy lies in the energy gap between the 3rd and 4th LLs of the top graphene electrode, see blue arrow in Fig. 3c. In contrast, a peak in conductance is observed for electrons tunnelling with conservation of energy, red arrow in Fig. 3c, because the 3rd LL in the bottom electrode is aligned in energy with the 4th LL in the top electrode. A slightly higher bias voltage brings into alignment the reduced energy of the inelastic tunnelling electron with an unoccupied state in the 4th LL in the top electrode, resulting in a peak in conductance, Fig 3d. In order to demonstrate the effect of the temperature-dependent change in the relative contributions

of these two processes, we show in Fig. 3b a colour map of conductance calculated using a model developed previously for phonon assisted¹⁸ inter-LL tunnelling²² in a device with a non-magnetic hBN barrier. The model includes the two competing processes: inelastic tunnelling processes induced by a single magnon with an energy of 10 meV and a scattering amplitude, $\propto 1 - f(T)$, which decreases as the temperature increases through T_c ; and elastic tunnelling processes whose amplitude, $\propto f(T)$, increases as temperature increases. The model is in qualitative agreement with measured data, see Figs. 3a and b.

We suggest that this type of ferromagnetic tunnelling barrier could be used to inject spin polarized carriers into a graphene layer or a related van der Waals layer. For the case when the emitter and collector states are displaced in momentum space (as for twisted graphene lattices or for two materials with different lattice periodicity), conservation of in-plane momentum can be enabled by the emission of magnons, which select only one spin polarization. The use of ferromagnetic tunnel barriers could therefore enrich the type and functionality of future van der Waals heterostructures.

Methods

Fabrication

CrBr₃ crystals were purchased from a commercial supplier: HQ graphene.

CrBr₃ was first exfoliated onto a polypropylene carbonate (PPC) coated SiO₂/Si substrate in an argon-filled glove box maintaining water and oxygen concentration less than 0.1ppm. CrBr₃ flakes of different thicknesses (2 to 6 layers) were identified by using the contrast variation under different colour filters and dark field imaging. Heterostructures comprising SLG/CrBr₃/SLG encapsulated within thin boron nitride (BN) layers were assembled on a 290 nm SiO₂/Si substrate following standard dry transfer procedure using a PMMA membrane. First, a single layer graphene (SLG) was picked up by a thin boron nitride layer (~8-10 nm BN) using the PMMA membrane. Subsequently, a suitable CrBr₃ layer was picked up by SLG/BN/PMMA membrane in the glove box. Finally, this stack of CrBr₃/SLG/BN/ on the PMMA membrane was peeled onto the SLG/BN/290 nm SiO₂/Si substrate. The final stack consists of Si/ 290nm SiO₂/ ~25nm BN/ SLG/ CrBr₃/ SLG/ ~ 10nm BN.

For electrical characterization of the tunnelling devices, Cr/Au edge contacts were made on the top and bottom graphene layers using electron beam lithography followed by boron nitride etching, metal deposition and lift-off process. Boron nitride was etched in a reactive ion etching system using CHF₃ and oxygen chemistry. Contacts on the graphene sheets were made so as to have four probe measurement geometry. Note that during the heterostructure assembly, the top and bottom graphene layers were chosen to extend beyond the CrBr₃ layer so that the contact processing (especially top BN etching and subsequent lift-off process) does not affect the CrBr₃.

Modelling

The magnon density of states was calculated in the nearest-neighbour approximation with the values of exchange integrals $J=1.698\text{mV}$ and $J_L=0.082\text{mV}$ taken from the experiment^{34,35}. Temperature and magnetic field dependences of the magnon spectra were calculated within the self-consistent spin-wave theory²⁴. The details are presented in the Supplemental Information.

Acknowledgements

This work was supported by EU Graphene Flagship Program, European Research Council Synergy Grant Hetero2D, the Royal Society, Engineering and Physical Research Council (UK), US Army Research Office (W911NF-16-1-0279).

Remarks

During the preparation of the manuscript the authors became aware of similar work done using a different chromium-trihalide (CrI₃)³⁶⁻³⁸.

References

- 1 Novoselov, K. S. *et al.* Two-dimensional atomic crystals. *Proc. Natl. Acad. Sci. USA* **102**, 10451-10453, doi:10.1073/pnas.0502848102 (2005).
- 2 Novoselov, K. S. Nobel Lecture: Graphene: Materials in the Flatland. *Rev. Mod. Phys.* **83**, 837-849, doi:10.1103/RevModPhys.83.837 (2011).
- 3 Butler, S. Z. *et al.* Progress, challenges, and opportunities in two-dimensional materials beyond graphene. *ACS Nano* **7**, 2898-2926, doi:10.1021/nn400280c (2013).
- 4 Geim, A. K. & Grigorieva, I. V. Van der Waals heterostructures. *Nature* **499**, 419-425, doi:10.1038/nature12385 (2013).
- 5 Novoselov, K. S., Mishchenko, A., Carvalho, A. & Castro Neto, A. H. 2D materials and van der Waals heterostructures. *Science* **353**, aac9439-aac9439, doi:10.1126/science.aac9439 (2016).
- 6 Dean, C. *et al.* Graphene based heterostructures. *Solid State Communications* **152**, 1275-1282, doi:10.1016/j.ssc.2012.04.021 (2012).
- 7 Lee, G. H. *et al.* Electron tunneling through atomically flat and ultrathin hexagonal boron nitride. *Appl. Phys. Lett.* **99**, 243114, doi:10.1063/1.3662043 (2011).
- 8 Amet, F. *et al.* Tunneling spectroscopy of graphene-boron-nitride heterostructures. *Phys. Rev. B* **85**, 073405, doi:10.1103/PhysRevB.85.073405 (2012).
- 9 Britnell, L. *et al.* Electron tunneling through ultrathin boron nitride crystalline barriers. *Nano Lett.* **12**, 1707-1710, doi:10.1021/nl3002205 (2012).
- 10 Mishchenko, A. *et al.* Twist-controlled resonant tunnelling in graphene/boron nitride/graphene heterostructures. *Nat. Nanotechnol.* **9**, 808-813, doi:10.1038/nnano.2014.187 (2014).
- 11 Wallbank, J. R. *et al.* Tuning the valley and chiral quantum state of Dirac electrons in van der Waals heterostructures. *Science* **353**, 575-579, doi:10.1126/science.aaf4621 (2016).
- 12 Wang, H., Eyert, V. & Schwingenschlogl, U. Electronic structure and magnetic ordering of the semiconducting chromium trihalides CrCl₃, CrBr₃, and CrI₃. *Journal of Physics-Condensed Matter* **23**, 116003, doi:10.1088/0953-8984/23/11/116003 (2011).
- 13 Sachs, B., Wehling, T. O., Novoselov, K. S., Lichtenstein, A. I. & Katsnelson, M. I. Ferromagnetic two-dimensional crystals: Single layers of K₂CuF₄. *Phys. Rev. B* **88**, 201402, doi:10.1103/PhysRevB.88.201402 (2013).
- 14 Zhang, W. B., Qu, Q., Zhua, P. & Lam, C. H. Robust intrinsic ferromagnetism and half semiconductivity in stable two-dimensional single-layer chromium trihalides. *J. Mater. Chem. C* **3**, 12457-12468, doi:10.1039/c5tc02840j (2015).
- 15 Liu, J. Y., Sun, Q., Kawazoe, Y. & Jena, P. Exfoliating biocompatible ferromagnetic Cr-trihalide monolayers. *Phys. Chem. Chem. Phys.* **18**, 8777-8784, doi:10.1039/c5cp04835d (2016).

- 16 McGuire, M. A., Dixit, H., Cooper, V. R. & Sales, B. C. Coupling of crystal structure and magnetism in the layered, ferromagnetic insulator CrI₃. *Chem. Mat.* **27**, 612-620, doi:10.1021/cm504242t (2015).
- 17 Huang, B. *et al.* Layer-dependent ferromagnetism in a van der Waals crystal down to the monolayer limit. *Nature* **546**, 270-+, doi:10.1038/nature22391 (2017).
- 18 Vdovin, E. E. *et al.* Phonon-assisted resonant tunneling of electrons in graphene-boron nitride transistors. *Phys. Rev. Lett.* **116**, 186603, doi:10.1103/PhysRevLett.116.186603 (2016).
- 19 Jung, S. *et al.* Vibrational properties of h-BN and h-BN-graphene heterostructures probed by inelastic electron tunneling spectroscopy. *Sci. Rep.* **5**, 16642, doi:10.1038/srep16642 (2015).
- 20 Chandni, U., Watanabe, K., Taniguchi, T. & Eisenstein, J. P. Signatures of phonon and defect-assisted tunneling in planar metal-hexagonal boron nitride-graphene junctions. *Nano Lett.* **16**, 7982-7987, doi:10.1021/acs.nanolett.6b04369 (2016).
- 21 Chandni, U., Watanabe, K., Taniguchi, T. & Eisenstein, J. P. Evidence for defect-mediated tunneling in hexagonal boron nitride-based junctions. *Nano Lett.* **15**, 7329-7333, doi:10.1021/acs.nanolett.5b02625 (2015).
- 22 Greenaway, M. T. *et al.* Resonant tunnelling between the chiral Landau states of twisted graphene lattices. *Nat. Phys.* **11**, 1057-1062, doi:10.1038/nphys3507 (2015).
- 23 Tsui, D. C., Dietz, R. E. & Walker, L. R. Multiple magnon excitation in NiO by electron tunneling. *Phys. Rev. Lett.* **27**, 1729-1732, doi:10.1103/PhysRevLett.27.1729 (1971).
- 24 Samuelsen, E. J., Silbergliitt, R., Shirane, G. & Remeika, J. P. Spin waves in ferromagnetic CrBr₃ studied by inelastic neutron scattering. *Physical Review B-Solid State* **3**, 157-166, doi:10.1103/PhysRevB.3.157 (1971).
- 25 Yelon, W. B. & Silbergliitt, R. Renormalization of large-wave-vector magnons in ferromagnetic CrBr₃ studied by inelastic neutron scattering: spin-wave correlation effect. *Physical Review B-Solid State* **4**, 2280-2286, doi:10.1103/PhysRevB.4.2280 (1971).
- 26 Irkhin, V. Y., Katanin, A. A. & Katsnelson, M. I. Self-consistent spin-wave theory of layered Heisenberg magnets. *Phys. Rev. B* **60**, 1082-1099, doi:10.1103/PhysRevB.60.1082 (1999).
- 27 Ho, J. T. & Litster, J. D. Magnetic equation of state of CrBr₃ near critical point. *Phys. Rev. Lett.* **22**, 603-606, doi:10.1103/PhysRevLett.22.603 (1969).
- 28 Ghannadzadeh, S. *et al.* Simultaneous loss of interlayer coherence and long-range magnetism in quasi-two-dimensional PdCrO₂. *Nat. Commun.* **8**, 15001, doi:10.1038/ncomms15001 (2017).
- 29 De Gennes, P. G. & Friedel, J. Anomalies de resistivite dans certains metaus magnetiques. *Journal of Physics and Chemistry of Solids* **4**, 71-77, doi:10.1016/0022-3697(58)90196-3 (1958).
- 30 Haas, C. Spin-disorder scattering and magnetoresistance of magnetic semiconductors. *Phys. Rev.* **168**, 531-538, doi:10.1103/PhysRev.168.531 (1968).
- 31 Irkhin, V. Y. & Katsnelson, M. I. Current carriers in a quantum 2-dimensional antiferromagnet. *Journal of Physics-Condensed Matter* **3**, 6439-6453, doi:10.1088/0953-8984/3/33/021 (1991).
- 32 Korenblit, I. Y. & Lazarenko, Y. P. Electron-magnon interaction in ferromagnetic semiconductors. *Phys. Status Solidi B-Basic Res.* **71**, K107-K110, doi:10.1002/pssb.2220710166 (1975).
- 33 Gantmakher, V. F. & Levinson, Y. B. *Carrier Scattering in metals and semiconductors*. 459 (North Holland, 1987).
- 34 Kresse, G. & Furthmuller, J. Efficient iterative schemes for ab initio total-energy calculations using a plane-wave basis set. *Phys. Rev. B* **54**, 11169-11186, doi:10.1103/PhysRevB.54.11169 (1996).
- 35 Kresse, G. & Joubert, D. From ultrasoft pseudopotentials to the projector augmented-wave method. *Phys. Rev. B* **59**, 1758-1775, doi:10.1103/PhysRevB.59.1758 (1999).

- 36 Dahlia R. Klein, et. al. Probing magnetism in 2D van der Waals crystalline insulators via electron tunneling. arXiv:1801.10075 (2018).
- 37 Tiancheng Song, et. al. Giant Tunneling Magnetoresistance in Spin-Filter van der Waals Heterostructures. arXiv:1801.08679 (2018).
- 38 Zhe Wang, et.al. Very Large Tunneling Magnetoresistance in Layered Magnetic Semiconductors CrI_3 . arXiv:1801.08188 (2018).

Supplementary Information

Magnon-assisted tunnelling in van der Waals heterostructures based on CrBr₃

D. Ghazaryan¹, M.T. Greenaway², Z. Wang¹, V.H. Guarochico-Moreira^{1,3}, I.J. Vera-Marun¹, J. Yin¹, Y. Liao¹, S. V. Morozov^{4,5}, O. Kristanovski⁶, A. I. Lichtenstein⁶, M. I. Katsnelson⁷, F. Withers⁸, A. Mishchenko^{1,9}, L. Eaves^{1,10}, A. K. Geim^{1,9}, K. S. Novoselov^{1,9,}, A. Misra¹*

¹*School of Physics and Astronomy, University of Manchester, Oxford Road, Manchester, M13 9PL, UK*

²*Department of Physics, Loughborough University, Loughborough, LE11 3TU, UK*

³*Escuela Superior Politécnica del Litoral, ESPOL, Facultad de CNM, Campus Gustavo Galindo Km 30.5 Vía Perimetral, P.O. Box 09-01-5863, Guayaquil, Ecuador*

⁴*Institute of Microelectronics Technology and High Purity Materials, RAS, Chernogolovka, 142432, Russia*

⁵*National University of Science and Technology “MISiS”, 119049, Leninsky pr. 4, Moscow, Russia*

⁶*Institute of Theoretical Physics, University Hamburg, D-20355, Hamburg, Germany*

⁷*Institute for Molecules and Materials, Radboud University, 6525AJ, Nijmegen, Netherlands*

⁸*University of Exeter, College of Engineering, Mathematics and Physical Sciences, Exeter EX4 4SB, Devon, England*

⁹*National Graphene Institute, University of Manchester, Oxford Road, Manchester, M13 9PL, UK*

¹⁰*School of Physics and Astronomy, University of Nottingham, Nottingham, NG7 2RD, UK*

S1. Device fabrication

S2. Temperature dependence of differential dI/dV_b conductance on magnetic field for devices with different thickness of CrBr₃

S3. Quantum capacitance of Gr/CrBr₃/Gr devices

S4. Calculation of magnon density of states

S1. Device fabrication

Several devices with a different number of CrBr_3 layers (2 to 6) were fabricated. Fig. S1 depicts the procedure for fabricating a device with 4 layers of CrBr_3 .

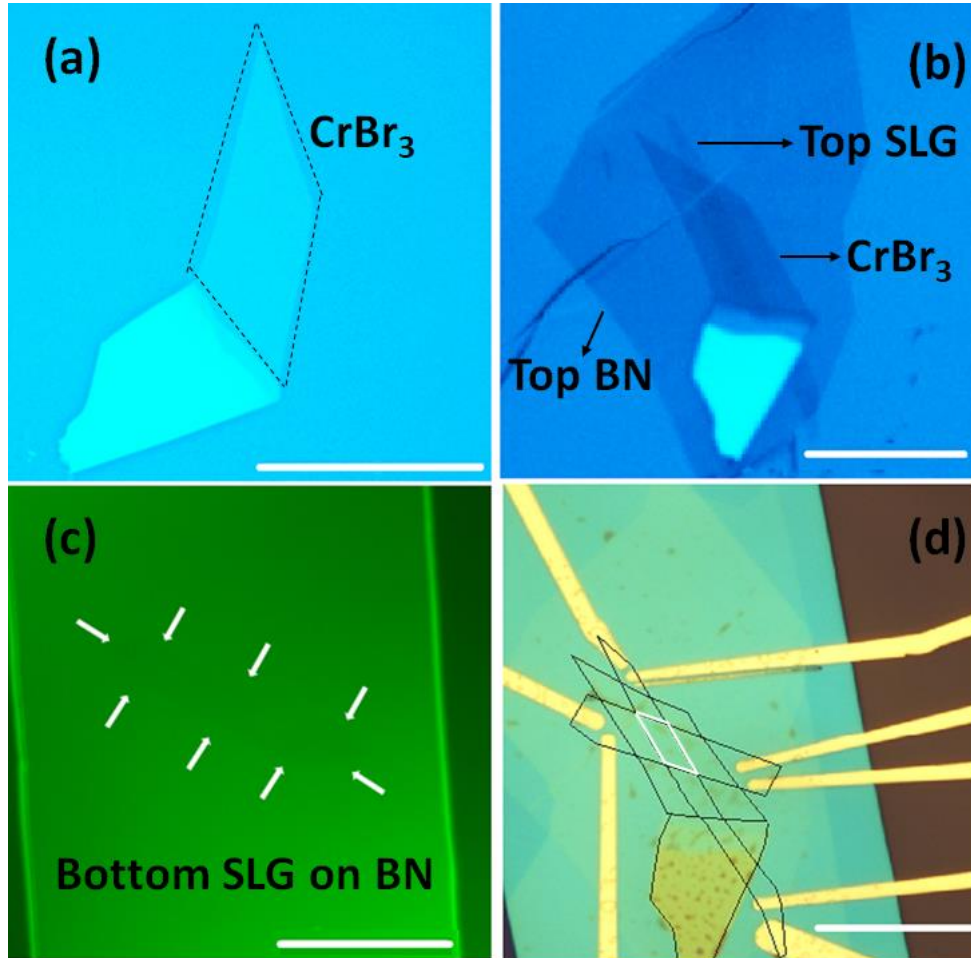


Fig.S1. Optical images of SLG/ CrBr_3 /SLG tunnel device encapsulated with hBN during different fabrication steps. **a**, 4 layers CrBr_3 flake (marked by black dashed line). **b**, CrBr_3 /SLG/top BN picked up on PMMA membrane (SLG – single layer graphene). **c**, SLG (marked by the white arrows) transferred on bottom hBN. After this, the stack shown in **b**, was transferred on the SLG/BN/ SiO_2 /Si shown in **c**. **d**, BN encapsulated SLG/ CrBr_3 /SLG stack with deposited Cr/Au contacts. Black lines represent different layers and white parallelogram marks the actual tunnelling area. Scale bars in all images are 20 μm .

S2. Temperature dependence of differential dI/dV_b conductance on magnetic field for devices with different thickness of CrBr_3

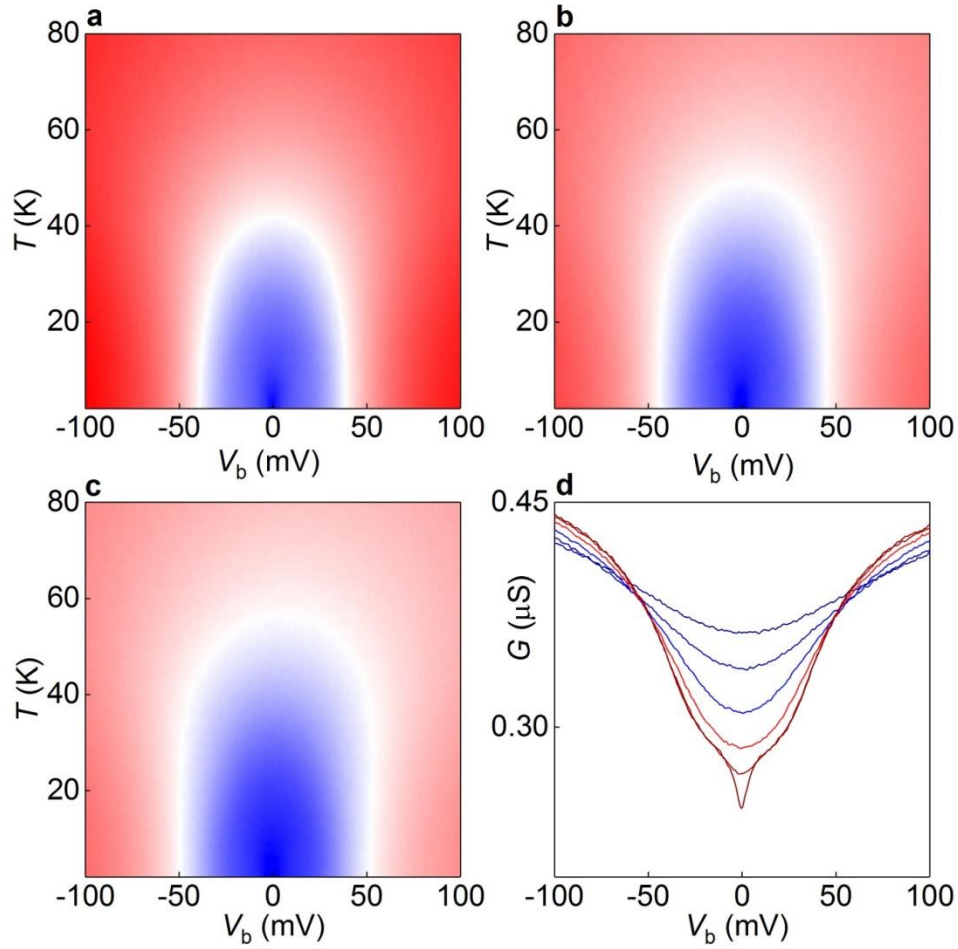


Fig. S2. **a**, Differential tunnel conductance as a function of V_b and T at $B_{||}=0\text{T}$ and $V_g=0\text{V}$ for a device with 2 layer thick CrBr_3 tunnel barrier (colour scale blue to white to red, $244\mu\text{S}$ to $343\mu\text{S}$ to $443\mu\text{S}$ for all contour plots in the figure). **b**, Similar to **a**, except $B_{||}=10\text{T}$. **c**, Similar to **a**, except $B_{||}=17.5\text{T}$. **d**, Zero-field tunnel conductance plots for various temperatures at a fixed gate voltage of $V_g=0\text{V}$ (blue to purple curves range from $T=2\text{K}$ to $T=50\text{K}$ with the step 10K).

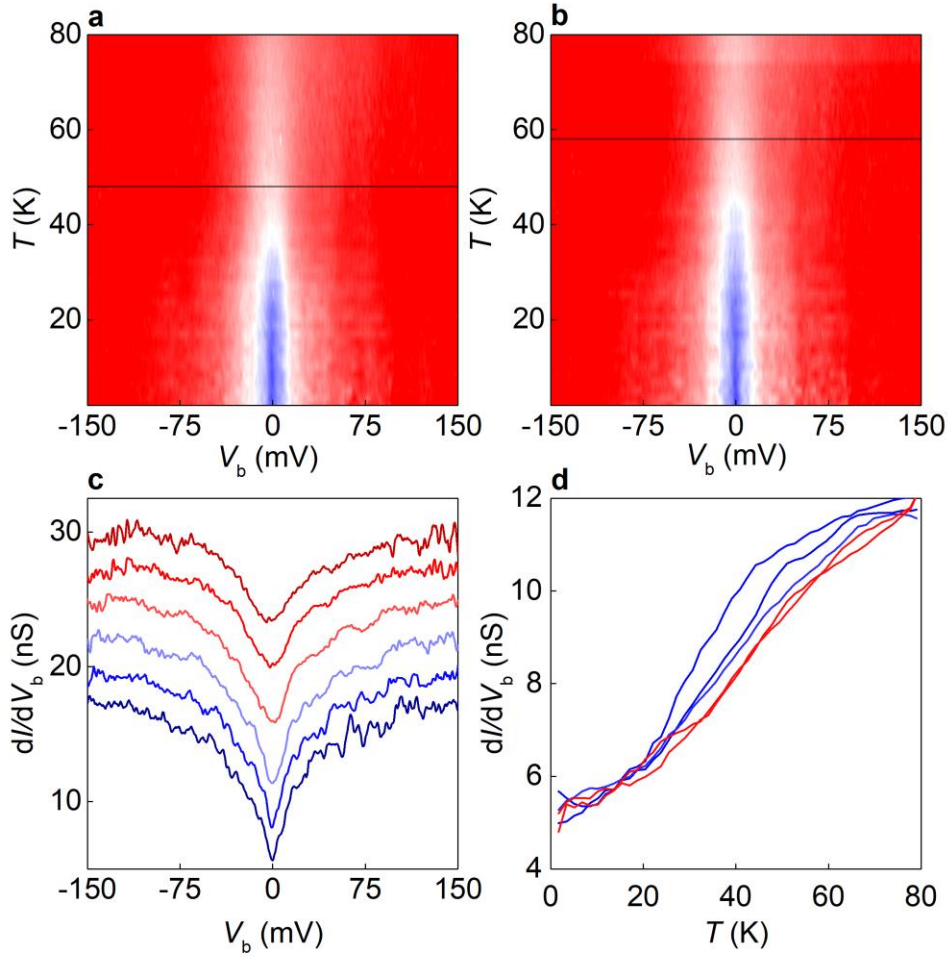


Fig. S3. **a**, Differential tunnel conductance as a function of V_b and T at $B_{||}=0$ T and $V_g=0$ V for a device with a 6-layer thick CrBr_3 tunnel barrier (colour scale blue to white to red, 3 nS to 9.25 nS to 16.5 nS for all contour plots in the figure). Black horizontal lines in a,b mark the position of the extracted value of T_c . **b**, Similar to a, except $B_{||}=10$ T. **c**, Zero-field tunnel conductance plots for various temperatures at a fixed gate voltage, $V_g=0$ V (blue to purple curves range from 2 K to 50 K in steps of 10 K, curves are shifted vertically for clarity). **d**, Dependence of the zero bias tunneling conductance dI/dV_b on T for different $B_{||}$ (red to blue curves are $B_{||}=0$ T, 5 T, 10 T, 15 T, 17.5 T).

S3. Quantum capacitance of $Gr/CrBr_3/Gr$ devices

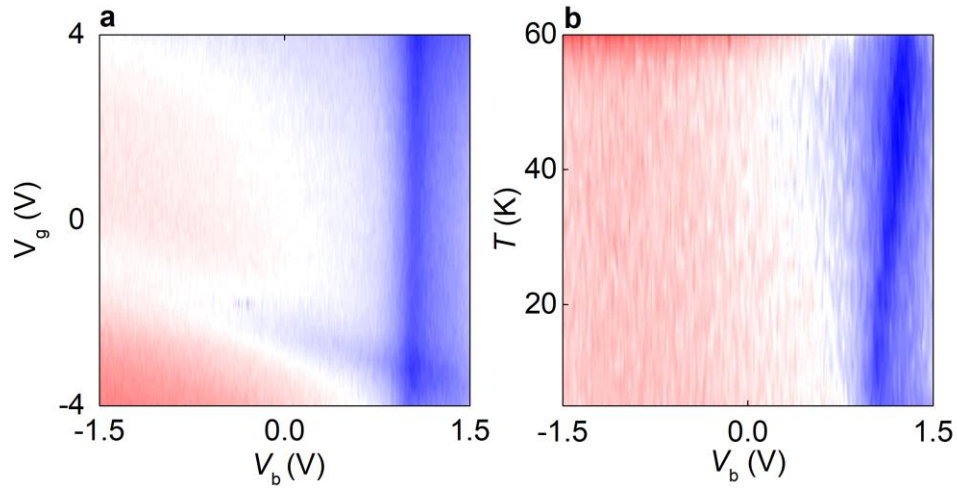


Fig. S4. Quantum capacitance measurements of the top gated $Gr/CrBr_3/Gr$ device (fabricated on quartz substrate). $CrBr_3$ thickness 15nm, cross-section area $100\mu m^2$. **a**, Capacitance as a function of V_b and V_g at $T=2K$ and zero magnetic field (colour scale blue to white to red, 0.23pF to 0.24pF to 0.25pF). Two blue regions correspond to the suppressed density of states near the Dirac points of the top and bottom graphene layers. The edge of the blue region for the bottom layer is vertical, consistent with strong screening of the gate-induced electric field by the thick $CrBr_3$ barrier. **b**, the differential capacitance as a function of V_b and T at a fixed $V_g=0V$ voltage.

S4. Calculation of magnon density of states

To calculate renormalized magnon spectra at finite temperatures we use self-consistent spin-wave theory in the form suggested in Ref.[S1]. We modify it to the case of a hexagonal lattice. For a single layer, there are two magnetic atoms per elementary cell with the corresponding magnon annihilation operators b_1 and b_2 . The magnon spectrum is diagonalized by the same unitary transformation as for the electronic spectrum of graphene [S2],

$$b_{\vec{k}_1} = \frac{1}{\sqrt{2}}(\alpha_{\vec{k}_1} + \alpha_{\vec{k}_2}),$$

$$b_{\vec{k}_2} = \frac{S(\vec{k})}{\sqrt{2}f(\vec{k})}(\alpha_{\vec{k}_1} - \alpha_{\vec{k}_2})$$

where \vec{k} is the magnon wave vector, $S(\vec{k}) = \sum_{\vec{\delta}} e^{i\vec{k}\vec{\delta}}$, $\vec{\delta}$ are the nearest neighbour vectors and $f(\vec{k}) = |S(\vec{k})|$. The self-consistent magnon spectrum at finite temperatures is determined by the two parameters, γ, γ_L characterizing the renormalization of in-plane and out-of-plane exchange integrals (J and J_L), respectively. The two magnon branches are:

$$E_{\vec{k}_{1,2}} = 2J\gamma(3 \mp f(\vec{k})) + 2J_L\gamma_L(1 - \cos k_z c) - \mu,$$

where c is the interlayer distance and μ is the magnon chemical potential which is nonzero above the Curie temperature. The self-consistent equations for the parameters γ, γ_L and the average spin per site \bar{S} are

$$\gamma = \bar{S} + \frac{1}{6} \sum_{\vec{k}} f(\vec{k}) [N_B(E_{\vec{k}_1}) - N_B(E_{\vec{k}_2})]$$

$$\gamma_L = \bar{S} + \frac{1}{2} \sum_{\vec{k}} [N_B(E_{\vec{k}_1}) + N_B(E_{\vec{k}_2})] \cos k_z c$$

$$\bar{S} = S + (2S + 1)N_B(E_f) - \frac{1}{2} \sum_{\vec{k}} [N_B(E_{\vec{k}_1}) + N_B(E_{\vec{k}_2})]$$

where $E_f = (2S + 1)(6J\gamma + 2J_L\gamma_L - \mu)$ and $N_B(E) = \frac{1}{\exp(E/k_B T) - 1}$ is the Bose Einstein distribution function.

The computational results are shown in Fig.S5. The calculations show that the effective magnetic coupling between the layers characterized by the parameter γ_L disappears near the Curie temperature whereas the short-range order in-plane characterized by the parameter γ survives to higher temperatures, as expected for quasi-two-dimensional magnets [S3].

The in-plane correlation length $\xi(T)$ can be estimated from the effective spin-wave spectrum above the Curie temperature,

$$E(\vec{k}) = D \left(k^2 + \frac{1}{\xi^2} \right),$$

where D is the spin-wave stiffness constant. For the particular case of the honeycomb lattice in the nearest-neighbour approximation

$$a / \xi(T) = \sqrt{\frac{2|\mu|}{3J\gamma}},$$

where a is the distance between the neighbouring magnetic ions. The computational results are shown in Fig. S6.

The self-consistent spin-wave theory does not give a very accurate estimate of T_c , but is rather an upper estimate. Fluctuation corrections will lower the value of T_c by a factor ~ 1.5 [S1]. Therefore, in our comparison of the theory with experiment, we have shifted the temperature dependence of calculated variables by the calculated value of T_c but keeping the same ratio of J/J_L .

To consider how the magnetic field B affects the magnon spectrum, one needs to replace $-\mu$ by the Zeeman gap $2\mu_B B$, where μ_B is the Bohr magneton, in all the above equations. Self-consistent solution of the equations for our parameters gives us the shift of magnon energy peaks with the slope being between $4.5 \cdot \mu_B$ V/T and $7.1 \cdot \mu_B$ V/T depends on two Van Hove singularities at temperature close to T_c (Figure S7).

Within the self-consistent spin-wave theory, the intensity of the two-magnon processes (one magnon is emitted and one magnon is adsorbed) with the total energy change close to zero and the total wave vector change equal to \vec{q} is proportional to the corresponding contribution to the longitudinal spectral density and reads [S4]

$$K_{\vec{q}}(T, H) = \sum_{\vec{k}} N_{\vec{k}} (1 + N_{\vec{k}+\vec{q}}) \delta(E_{\vec{k}} - E_{\vec{k}+\vec{q}})$$

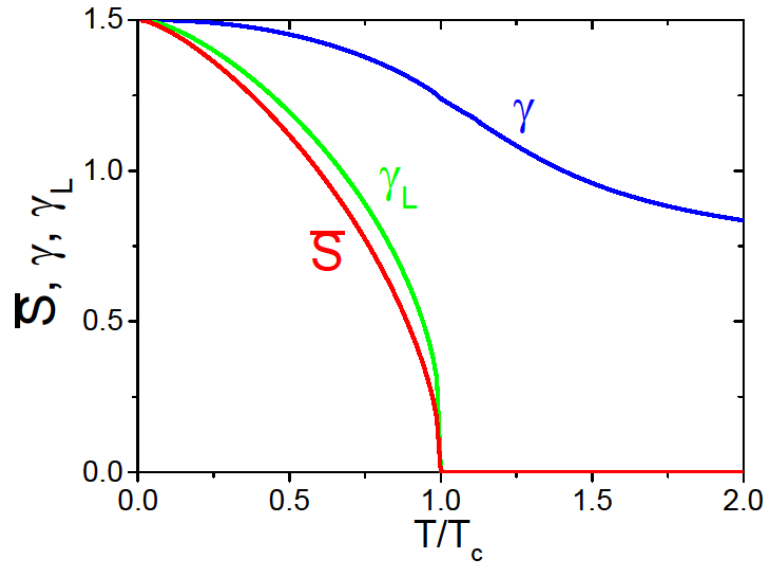


Figure S5. Temperature dependences of $\bar{S}, \gamma, \gamma_L$ at zero magnetic field.

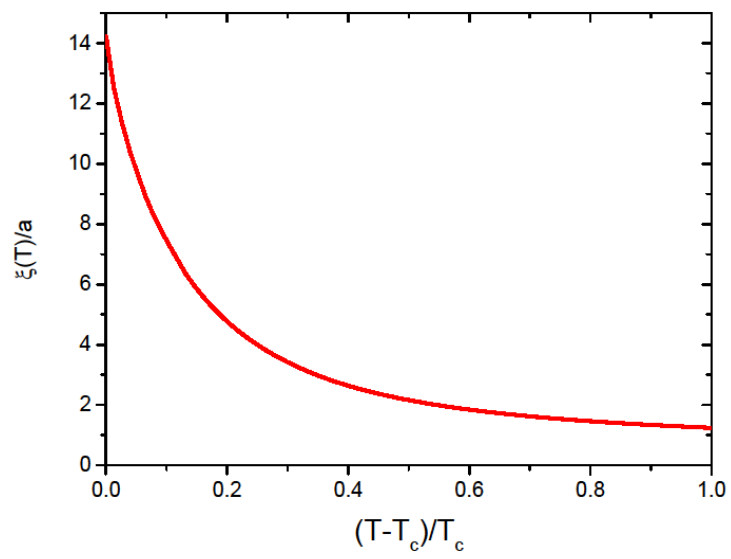


Figure S6. Temperature dependence of $\xi(T)/a$.

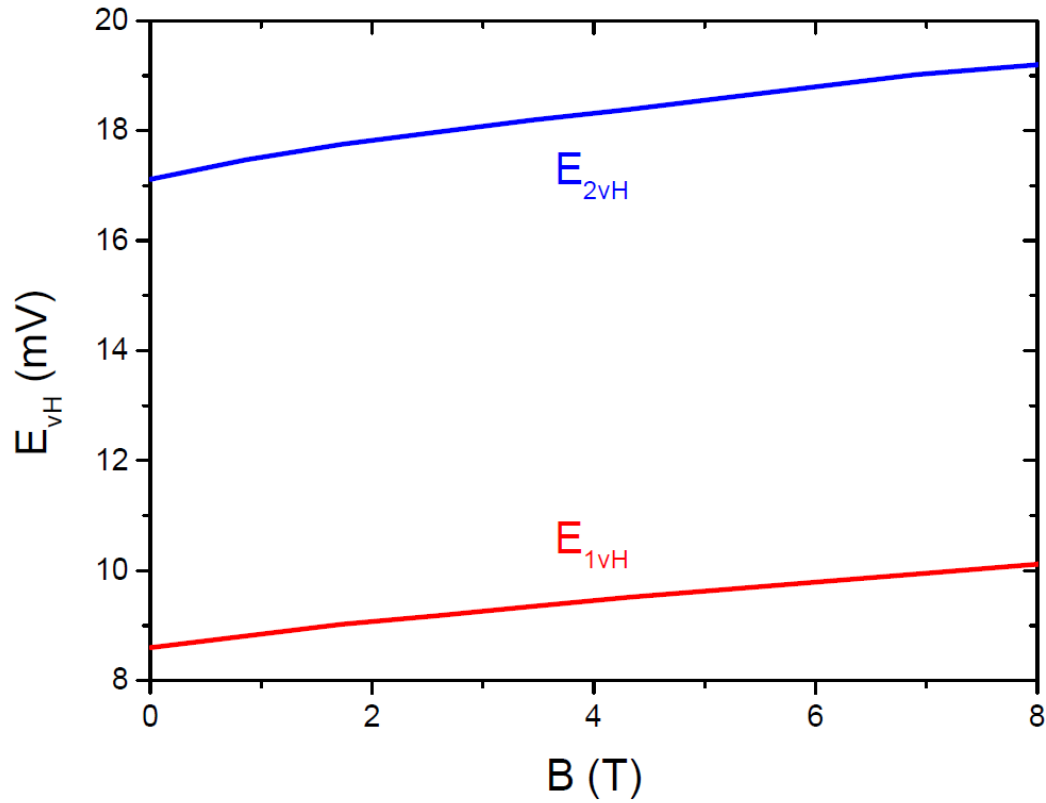


Figure S7. Magnetic field dependence of the positions of van Hove singularities in magnon spectrum.

Supplementary References

- [S1] Irkhin, V. Y., Katanin, A. A. & Katsnelson, M. I. Self-consistent spin-wave theory of layered Heisenberg magnets. *Phys. Rev. B* **60**, 1082-1099, doi:10.1103/PhysRevB.60.1082 (1999).
- [S2] Katsnelson, M. I. Graphene: Carbon in Two Dimensions (Cambridge Univ, Press, Cambridge, 2012)
- [S3] Ghannadzadeh, S. *et al.* Simultaneous loss of interlayer coherence and long-range magnetism in quasi-two-dimensional PdCrO₂. *Nat. Commun.* **8**, 15001, doi:10.1038/ncomms15001 (2017).
- [S4] Irkhin, V. Yu. & Katsnelson, M. I. Current carriers in a quantum two-dimensional magnets, *J. Phys.: Cond. Mat.* **3**, 6439-6453, doi:10.1088/0953-8984/3/33/021 (1991).